nature communications

Article

https://doi.org/10.1038/s41467-025-61809-8

Beaded metamaterials

Received: 28 May 2024

Accepted: 2 July 2025

Published online: 25 August 2025

Check for updates

Lauren Dreier[1], Trevor J. Jones[2,3], Abigail Plummer[4,5], Andrej Košmrlj[4,6] & P.-T. Brun[2,7]

Beading transforms flexible fiber networks into load-bearing structures by incorporating rigid, discrete elements in programmable weave patterns. Beaded assemblies function as mechanical metamaterials, where emergent mechanical behaviors arise from the interplay between geometry and material properties. Here, we investigate how this interplay governs the global mechanics of bead-thread networks. Using a combination of experiment and simple modeling, we identify conditions under which beaded structures undergo superjamming – a mechanically locked state that dramatically enhances load capacity. Our results show how potentially limiting factors such as gravity and friction can be leveraged to extend the domain of soft materials design into applications that demand rigidity.

Worn close to the body or stretched overhead as a roof, textiles are known for their softness and versatility. Their tendency towards compliance can be explained by the fibers they are made from, which bend easily due to their slender geometry. Geometry also contributes to textile mechanics when fibers are manipulated—by hand, machine, or nature—into hierarchical structures[1], giving way to new and sometimes surprising properties. For example, inelastic yarns can become effectively elastic by knitting them into a stretchable fabric, and discrete layers of wool fabric can cohere without glue or stitching by felting. A material that exhibits emergent global behavior by leveraging its structure is known as a *mechanical metamaterial*[2]. Classified as such, materials as ancient and commonplace as weaves and knits are currently being examined in a new light, propelled by the recent paradigm shift towards understanding and ultimately harnessing nonlinear mechanics such as elastic buckling[3,4] and plasticity[5]. Progress has been made in characterizing the relationship between mechanical properties and fiber topology, including knits[6], knots[7,8], yarns[9], woven lattices[10–13], and non-woven fiber networks[14–16], in some cases using actuation (e.g., stimuli-responsive matter, pneumatics) to create functional shape-morphing matter with promising applications in wearable electronics[17–19] and soft micro robotics[20]. Traditional handicrafts with 2D architected geometry have also been reframed as mechanical metamaterials, including origami, kirigami[21], and pleating-like corrugations[22]. Like rod- and fiber-based materials, these systems also exhibit emergent mechanical properties and show potential for shape programming.

A major challenge in employing shape-morphable materials in real-world engineering scenarios lies in eliciting rigidity from materials that are otherwise soft, i.e., flexible enough to change shape without damage[23–25]. Granular systems close to the jamming transition demonstrate this dual behavior[26,27]. Jamming can be paired with compliant structures such as flexible membranes[28–30] and fiber elements[31] to gain functionality. Jamming particles can themselves be compliant and geometrically designed, leading to enhanced shock absorption[32]. However, jamming is typically a stochastic process and requires a positive form to prescribe shape. Tensegrity structures provide another framework for tunable stiffness and rigid shape morphing using struts that balance compression and tension. Applications in robotics[33] and meter-scale structures[34] are enabled by the manipulation of constituent elements, such as mechanically adjusting struts, cable tension, or cable length. While inherently efficient structures, tensegrity has a limited load-bearing capacity, can be sensitive to perturbations, and systematic design remains challenging[35,36]. Efforts have been made to combine mechanical principles from tensegrity and granular jamming by pairing rigid, volumetric elements with soft, elastic strings or membranes to produce energy-absorbing, multi-stable metamaterials[37]. Unlike classical tensegrity, the rigid elements are in contact, leading to dissipative behavior upon compression. Our work takes up *beadwork*, an ancient textile technique practiced by cultures around the world that uses continuous, often inextensible thread to link discrete, rigid, volumetric elements called beads. Continuous thread in beadwork prescribes

[1]School of Architecture, Princeton University, Princeton, NJ, USA. [2]Department of Chemical and Biological Engineering, Princeton University, Princeton, NJ, USA. [3]Department of Mechanical Engineering, Carnegie Mellon University, Pittsburgh, PA, USA. [4]Department of Mechanical and Aerospace Engineering, Princeton University, Princeton, NJ, USA. [5]Department of Mechanical Engineering, Boston University, Boston, MA, USA. [6]Princeton Materials Institute, Princeton University, Princeton, NJ, USA. [7]Department of Chemical Engineering, Soft Matter, Rheology and Technology, KU Leuven, Leuven, Belgium. e-mail: pierre-thomas.brun@kuleuven.be

https://doi.org/10.1038/s41467-025-61809-8

geometric order so that beaded objects take a fully programmed shape, while mechanically coupling elements through interactions involving friction, tension, and elasticity. Characterizing these mechanics specific to beaded materials becomes the subject of our study.

Beadwork draws on many fiber assembly techniques to create a wide range of designs, from simple 1D necklace-like configurations to fully 3D interlaced weaves. In this work, we study *angle weave* stitches due to their versatility in creating 2D and 3D designs (see Fig. 1a)[38–41]. In angle weaves, beads are woven in loops, forming interlaced rings of n beads that can cover a plane or 3D surface. Applying tension to the bead thread minimizes excess lengths between bead elements, reducing the packing fraction and inducing jamming. The beaded object thus takes a shape prescribed by the discrete tiling pattern of angle weave building blocks (see Fig. 1). If the pattern is designed with geometric frustration, such as the heptagonal tiling shown in Fig. 1a (iv), the tensioned beaded surface will not sit in-plane. In Fig. 1b, we show another design with geometric frustration: a half-dodecahedral shell comprised of intersecting loops of $n = 5$ beads. The assembly comes out-of-plane as tension is applied (see SI Video 1), lifting the blue and yellow beads off the surface. Clamping the ends in this state creates a scalable, rigid structure that can support the weight of an adult dancer—an unusual feature for soft materials. In Fig. 1b (iv) and SI Video 1, we show a 3D reconstruction of this model, obtained via micro-computed tomography (μ-CT). The solid acrylic beads in yellow appear translucent, revealing the more dense nitinol wire (blue) used as thread. For a simple, 20-bead object, the image reveals a tortuous mechanical system consisting of contacts between individual beads, beads with the thread, the thread with itself, and beads with supports. Despite these complexities, experiments demonstrate a consistent and tunable mechanical response, detailed in the next section.

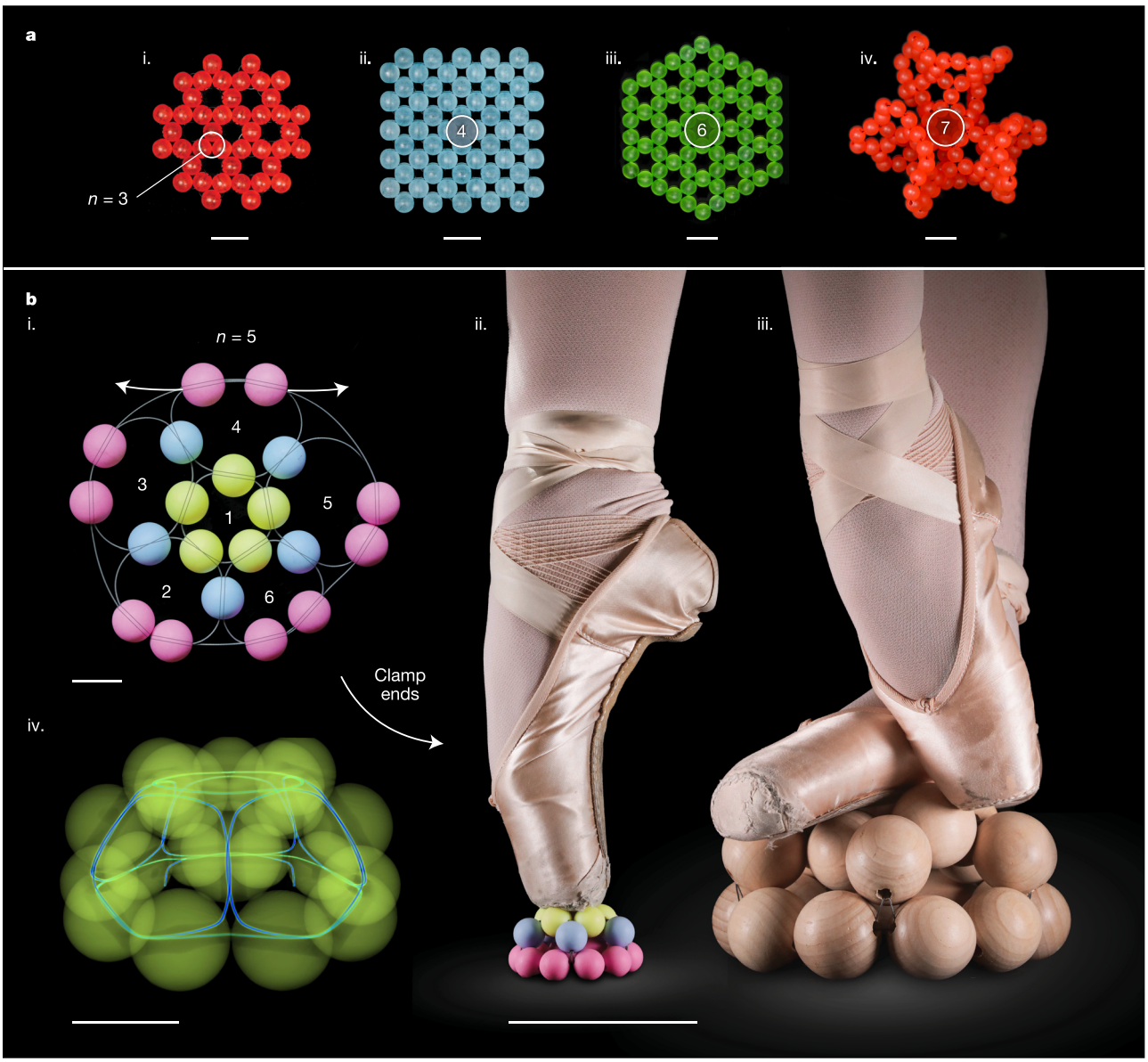

Fig. 1 | Design and emergent stiffness of objects beaded using an angle weave technique. a Sample angle-woven swatches comprised of adjoining loops of n beads, where $n = 3$–7. Non-Euclidean tiling of unit loops can lead to three-dimensional surfaces. Scale bars, 20 mm. **b** A beaded shell shown before tensioning (i), with thread pattern schematically traced over a photograph of otherwise opaque, 17 mm acrylic beads threaded with steel rope. Scale bar, 20 mm. Applying tension to the two free ends sends the half-dodecahedral shell out-of-plane (ii–iv). The structure becomes rigid across length scales by clamping the thread, capable of bearing large point (ii) and distributed (iii) loads. Scale bar, 100 mm. (iv), μ-CT reconstruction of the model of the same design using 10 mm acrylic beads (yellow) threaded with 0.25 mm nitinol wire (blue). Scale bar, 10 mm.

https://doi.org/10.1038/s41467-025-61809-8

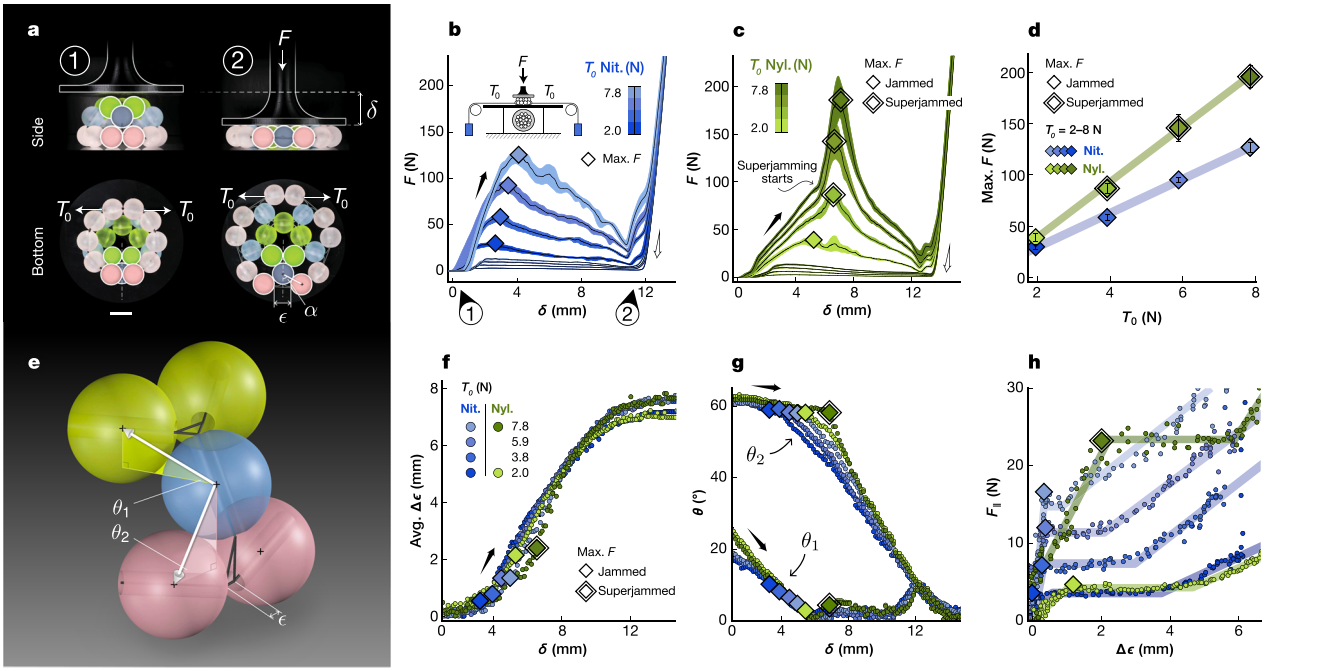

Fig. 2 | A beaded shell is compressed between two plates. a Photographs of the experiment. Constant tension (T_0) is applied to the thread ends as the indenter moves a distance δ. Shaded regions show the maximum and minimum force over all trials, and solid black lines show a moving average. Scale bar, 10 mm. **b** and **c** The force response (F) for identical shells threaded with different materials (0.25 mm diameter nitinol and 0.50 mm diameter nylon, respectively) as a function of δ, cycled three times across a range of T_0. Loading and unloading paths are marked with black and white arrows, respectively. **d** Maximum load as a function of tension for shells beaded with nitinol (blue) and nylon (green) thread. Maximum forces that occur in a superjammed regime are outlined. **e** Illustration of a 5-bead building block that comprises the model structure. Gray lines indicate bead hole orientation. **f** and **g** Tracking selected beads' motion over a single cycle across a range of T_0. **f** In-plane dilation of the bottom layer of beads measured by the length of exposed thread ($\Delta\epsilon$) as a function of δ. **g** Altitudinal angles θ_1 and θ_2 as a function of δ. **h** Projection of F as in-plane tension between two pink beads shown as a function of $\Delta\epsilon$. A 3-part piecewise linear fit is shaded behind each trial. The return path is not shown in (**f**–**h**). Source data is available in Supplementary Data 1.

Results

In Fig. 2, we characterize the compressive stiffness of our model system. We apply constant tension T_0 to the thread ends and compress the shell between two plates, as illustrated in Fig. 2a (see the "Methods" section, SI Video 2). In Fig. 2b, c we report the measured force F vs. indenter displacement δ for identical shells threaded with different materials: (b) nitinol (0.25 mm diameter) and (c) nylon (1 mm diameter). We identify several common features of the force response, as evident from the figure. First, the force to depress the shell increases until it reaches a maximum. The value of this maximum increases with the applied tension T_0. Second, after reaching a peak load, the shell softens so the indentation force decreases to nearly zero. The subsequent steep increase occurs when all the beads are flat on the substrate. Third, the return cycle has a large hysteresis, suggesting significant friction in the system[42]. Figure 2d confirms that the maximum force scales with tension. Results indicate a linear relationship between maximum force and tension across all trials. Notably, despite near-identical shells differing only in thread material, nylon trials exhibit 1.6 times greater maximum load than nitinol trials. This result is surprising given that nylon threads are elastically softer than nitinol wires (Young's moduli 1.80 ± 0.13 vs. 38.2 ± 3.2 GPa for nylon and nitinol, respectively). To understand this increased stiffness, we examine the data shown in Fig. 2c, where an additional, steeper slope emerges when loading nylon-threaded shells. In Fig. SI 2, we study our shell across different indenter shapes, materials, and bead radii. Our results show that, in addition to thread material, this regime is sensitive to indenter shape and bead roughness. Moreover, we can facilitate conditions for this behavior regardless of the thread material by clamping thread ends (see Figs. 1b iii–iv and SI 2d). In the clamped shells of Fig. SI 2d, the slopes with nitinol and nylon align in this regime (170 and 193 N/mm for nitinol and nylon, respectively), suggesting that mechanics shared by both shells, such as bead–bead and bead–support contacts—usurp thread elasticity. Accordingly, we call this regime *superjamming*, owing to its physical similarity to granular jamming and accounting for the enhanced load-bearing capability of the structure. Note that the shell response remains approximately the same across the material and geometric parameters we tested (see Fig. SI 2a–c), aside from this superjamming regime.

To probe deeper into the conditions for superjamming, we quantify shape change under load in Fig. 2e. We identify two primary metrics: in-plane dilation $\Delta\epsilon$ of the bottom ring comprised of pink beads, and the altitudinal angles θ_1 and θ_2 tracking the position of top (yellow) and bottom (blue) beads. These measurements are reported in Fig. 2f and g, respectively. Points of maximum force are overlayed, showing the geometric conformations that correspond with peak stiffness. Across all experiments, $\Delta\epsilon$ follows an S-curve, and the peak stiffness occurs on the lower branch. In other words, dilation of the bottom ring indicates shell softening and collapse. Looking at out-of-plane geometry, Fig. 2g shows that θ_1 quickly decreases to zero regardless of the applied tension or thread material. On the other hand, θ_2 remains approximately constant with increased tension. This stagnation is prolonged in the case of higher tension, causing a subtle rearrangement of the bead assembly with large consequences. In this limit, the indenter comes in direct contact with the blue beads, and the force path is vertical (see Fig. SI 3). This choreography of deformation maximizes the force for a given displacement, thereby causing the sudden slope change noticed in Fig. 2c. This superjammed configuration is maintained until the structure slips. We therefore associate superjamming with a 'locked' conformation that allows larger compressive forces before collapse. In Fig. 2h, we report the in-plane force resisted by tension in the bottom ring, $F_{\parallel}$ (see the "Methods" section). We recover three regimes: first, the dilation force increases linearly,

then plateaus near the moment the shell begins to soften, and finally increases again. The slopes of the first regime depend on the thread material (stiffer threads yield steeper slopes), and the plateaus scale with tension. This latter observation suggests that sliding friction plays a role in the integrity of the bottom ring[43].

These results establish a clear link between applied tension and load capacity and reveal that superjamming, a mechanically locked state, emerges only under specific material conditions. In particular, we associate superjamming with the suppression of dilation in the bottom ring, mediated by sliding friction. Yet the underlying cause of the shell's deformation sequence remains unresolved. To address this, we next examine the mechanics of a single ring—the fundamental building block of angle weave patterns—to isolate the roles of friction, geometry, and tension distribution in shaping global behavior.

In Fig. 3a, we show the force required to pull a thread through a single ring of n beads pretensioned by T_0, where n has the geometric effect of imposing kinks in the thread's path (see Fig. SI 4). We report the difference in tension between thread ends (see the "Methods" section). We find that the force first increases linearly and then gives way to a plateau of constant force, T^*. In Fig. 3b, we report the value of T^* that is found to scale linearly with T_0. The slopes are materially dependent but are found to be independent of the number of beads n. Leveraging this observation, we propose a first-order geometric model that ignores the thread's bending stiffness and nonlinear friction:

$$T^*/T_0 = e^{\mu_{\text{eff}}\phi}, \tag{1}$$

where μ is the effective frictional coefficient and $\phi = 2\pi$ for all n per capstan theory[44–46]. We find a fair agreement between Eq. (1) and our data, as highlighted by the collapse into lines reported in Fig. 3b. We obtain $\mu_{\text{eff}} = 0.11$ and 0.26 for nitinol and nylon, respectively. Nylon's nonlinearity at high tension is consistent with power-law friction often associated with polymeric materials, particularly in capstan configurations[47].

Next, we investigate the force to deform these beaded rings. In contrast to the previous experiment that examined thread friction through a fixed loop of beads, here the beads are free to slide as the planar ring is dilated by a spherical volume (shown in gray in the inset of Fig. 3c). In Fig. 3c, we report the force to press through a ring of $n = 3$, 4, and 5 beads under constant tension. After an initial, steep increase in force when making contact (point 1 in the figure), F gradually decreases to zero as the indenter aligns with the bead ring (point 2). Rescaling F by T_0, the data collapses into a single curve per thread type. We note that n does not affect F beyond geometric constraints (indenter-ring contact points are shown as dashed lines, see the "Methods" section). We use geometry to predict the response by performing a force balance across the indenter and a sample bead in the ring. We assume zero friction, constant tension throughout the network, and symmetric deformation as the ring is dilated. Despite these coarse assumptions, we find fair agreement with experimental results, where the prediction is slightly lower than the experimental data (white line in Fig. 3c versus blue and green points). We correct this error by incorporating friction through Eq. (1) and the experimentally derived μ_{eff} and find excellent agreement with experiments (blue and green lines for nitinol and nylon, respectively). Thus, we understand the deformation of a bead assembly near a free end: rigidity depends on the ability to prevent thread elongation by sliding, where deformation is mediated by the geometry of the network and the efficiency of load transfer across rigid contacts. Sliding also comes at the cost of capstan friction. To validate these claims, we can make a quantitative prediction of the maximum load supported by the shell initially introduced in Fig. 2. Here, we apply the geometric projection of Fig. 2h such that $\theta_2 = 60°$ and $\alpha = 0$ (see the "Methods" subsection "Dodecahedral shell ") and average capstan friction such that $\pi < \theta < 7\pi/5$ and $0.11 < \mu < 0.26$. We recover an equivalent scaling of the maximum load supported by the shell with no superjamming, i.e., ~10–20 times T_0, depending on the choice of thread.

Next, we extend our dilation experiment to a larger system and probe deeper into the weave. In Fig. 3d, we construct a 1D angle weave tiling that comprises 15 rings similar to those tested in Fig. 3a–c, but chained together with continuous thread (see the "Methods" section). We report the maximum dilation force F_{max} for sequential dilations performed along the chain ($i = 1$ denotes the ring closest to the free end). As expected, pretension T_0 affects the value of the maximum loads. Yet, results show that T_0 also dictates where peak stiffness occurs along the chain. These effects are exaggerated in nylon, where the stiffest ring approaches the free end when increasing pretension ($i = 5$ and $i = 2$ for $T_0 = 0.5$ or 16 N, respectively). After the peak, F_{max} decays and eventually plateaus at a characteristic value (~15 N in the ranges we tested). Importantly, nylon exhibits a shorter decay length than nylon. In all cases, F_{max} increases again at the boundary near $i = 15$.

To better understand the mechanisms underlying ring stiffness along the chain, we examine the in-plane dilation force $F_{\parallel}$ as a function of indenter displacement δ for each unit (see Fig. SI 5). Near the free end, we recover the now familiar capstan-like plot, consisting of an initial, linear regime and a plateau of constant force representing global slip, i.e., when the thread slides uniformly from the free end into the structure. As one could anticipate from capstan theory, the plateau height increases with the wrapping angle and thus with i. Deeper in the weave, this idealized scenario is no longer observed, suggesting that global slip does not occur. Instead, we argue that the excess length needed to open the ring is collected from the slack in the weave. As evident from Fig. SI 4, the thread length surrounding each ring increases from the free end.

Together, Figs. 3d and SI 5 highlight the central role of slack in shaping the mechanical behavior of larger bead-thread networks. In regions far from the free end, pretension alone no longer dictates stiffness; instead, the availability and distribution of slack become the dominant factors. This insight provides a unifying explanation for why certain shells of Fig. 2 exhibit superjamming while others do not. Previously, we have associated superjamming with a particular geometric condition, where the bottom ring resists deformation. This scenario is only possible when the bottom ring, closest to the free end, is stiffer than the units above it. Figure 3d is consistent with this argument, showing that increasing T_0 in the presence of friction and slack drives the stiffest cell towards the free end. Nitinol has lower friction than nylon, which attenuates these effects. As a result, the bottom ring always dilates first in nitinol for the range of T_0 we tested, preventing superjamming. To excite superjamming in nitinol, as seen in Fig. SI 2d, we clamp the ends as if supplying a very large T_0. Put simply, what matters in superjamming is the stiffness of cells relative to each other rather than the rigidity of the cells alone. Beyond superjamming, the mechanics far from the free end—where friction and, by extension, slack cannot be neglected—reveal fundamental behaviors that inform the design and performance of larger beaded networks, which we examine next.

In Fig. 4a–d, we continue our study of larger beaded networks with different geometries, subject to other means of deformation. In Fig. 4a, a column beaded with elastomeric thread is stretched and compressed axially. For small displacements, we observe a linear elastic response. In compression, the beads remain in contact so that the distance between bead centers is preserved. The thread is displaced to enable a more dense packing, where angle weave units are distorted from square-like shapes into rectangles (see Fig. 4b, i). Further compression yields superjamming. The beads stack vertically, and recorded forces become large despite the thread's softness. Note that Fu et al. recover a similar result[37], where spheres joined by discontinuous elastic threads eventually pack and jam when a compressive load is applied. In beading, thread continuity allows these structures to withstand tensile loading such that when stretched, the

https://doi.org/10.1038/s41467-025-61809-8

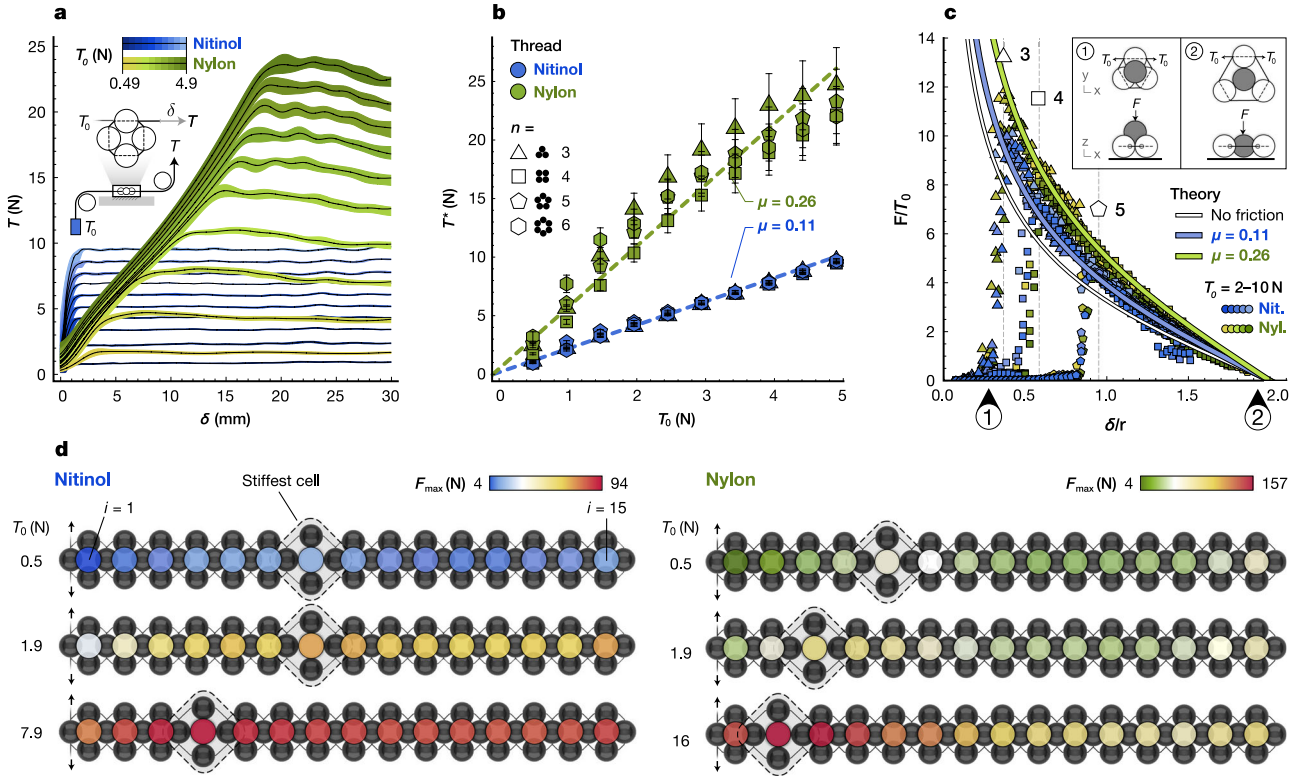

Fig. 3 | Decoupling (and recoupling) friction and geometry in beaded assemblies. a Measuring friction in a planar ring of $n = 4$ beads. A sliding thread is pulled through a loop of constrained beads for a displacement δ. Constant tension (T_0) is applied to one end of the thread while tension (T) is read at the other for a range of T_0 and two thread materials. **b** Kinetic friction plateaus T^* plotted as a function of T_0 for planar bead rings where n ranges from 3 to 6. Dashed lines indicate linear fits of the data. **c** Dimensionless force (F/T_0) vs. indenter displacement (δ) for dilating planar bead rings using a spherical-tipped indenter with the same radius as a bead. Experiments for $n = 3$, 4, and 5 are shown as n-sided markers. Theory for $n = 4$ and zero friction is drawn in white, with blue and green lines showing a correction for bead-thread friction in nitinol and nylon, respectively. **d** Maximum force to dilate sections of a planar chain of beads consisting of 15 adjoining rings of $n = 4$ beads, threaded with nitinol and nylon for various T_0. Source data is available in Supplementary Data 2.

beads move away from each other, but the structure remains intact (see Fig. 4b, iii). After a brief linear regime where slack is used up, we observe a strain-stiffening response. Similar behaviors are typically seen in other fibrous and fiber-like materials across scales, such as knit textiles[6], biological tissue[48], and polymers—often described by aptly named bead-spring models[49], based on the notion that slack exists in the system that can become exhausted; as a result, the comprising fiber-like elements are forced to stretch.

While slack may be viewed as a limiting and unavoidable factor in beaded materials, Fig. 4c, d show two examples of how slack and friction can be leveraged for functional behavior. First, slack can be modified after the structure has been woven by using stimuli-responsive materials. In Fig. 4c, we bead a rod ($n = 3$, 4) with shape-memory nitinol wire that shrinks uniformly in length by 2–5% when heated by electric current (see the "Methods" section)[50]. In a three-point bending test, we report that this relatively small strain increases the effective bending stiffness (known to scale linearly with F/δ[51]) by a factor of nearly two. In this sense, coupling beading with thread that changes length provides a promising path for expanding the application space of existing fiber actuators, often limited by their inherent softness[52,53].

Second, slack introduces internal degrees of freedom that enable reconfigurable mechanical responses, as demonstrated in Fig. 4d. Here, we assemble a domed shell from 20 mm diameter beads and waxed nylon thread (see the "Methods" section). To control curvature, we introduce disclination defects with coordination numbers $n = 5$ and $n = 7$ into an otherwise flat kagome lattice of $n = 6$ nodes. In regions away from defects where the local Gaussian curvature is near zero, the network is compliant under small displacements but stiffens significantly for larger ones. This behavior is consistent with Fig. SI 5 for $i \gg 1$, which shows that initial deformations draw from the available slack that is eventually used up. In the vicinity of $n = 5$ disclinations where intrinsic curvature is positive, the network is locally rigid even in the presence of slack. Under sufficient applied load, the local curvature can reverse orientation, resulting in a new shape. To quantify this threshold, in Fig. SI 6, we measure the force required to invert a single bistable cone formed from a hexagonal patch with a central defect ($n = 3$, 4, 5). The cone enters a superjamming regime prior to snapping, enhancing the energy barrier between bistable states. In the isolated cone models, thread ends are tied, forcing the network to accommodate inversion either by drawing from available slack or stretching. This mechanism, where local deformation stiffens remote regions, is consistent with prior observations of 1D beaded rods[54]. A similar but spatially attenuated effect is observed in the full shell structure. There, deformation leads to quasi-nonlocal stiffening: stress remains largely localized to the region surrounding the defect due to the combined effects of bead-thread friction and distributed slack. These features inhibit the propagation of tension across the entire network. As a result, the shell can undergo localized shape transformations while preserving rigidity elsewhere. This dual capacity for compliance and stabilization enables the material to access a continuum of rigid conformations maintained through external loads, internal constraints, and gravity.

To systematically control the number of possible conformations, reconfigurability can be discretized by beading an array of bistable cones. Figure 4e shows a design consisting of a diagonal square lattice of D-cones with defects of $n = 4$. Flipping each cone to an up (gray) or down (white) state alters the local curvature, enabling a palette with

https://doi.org/10.1038/s41467-025-61809-8

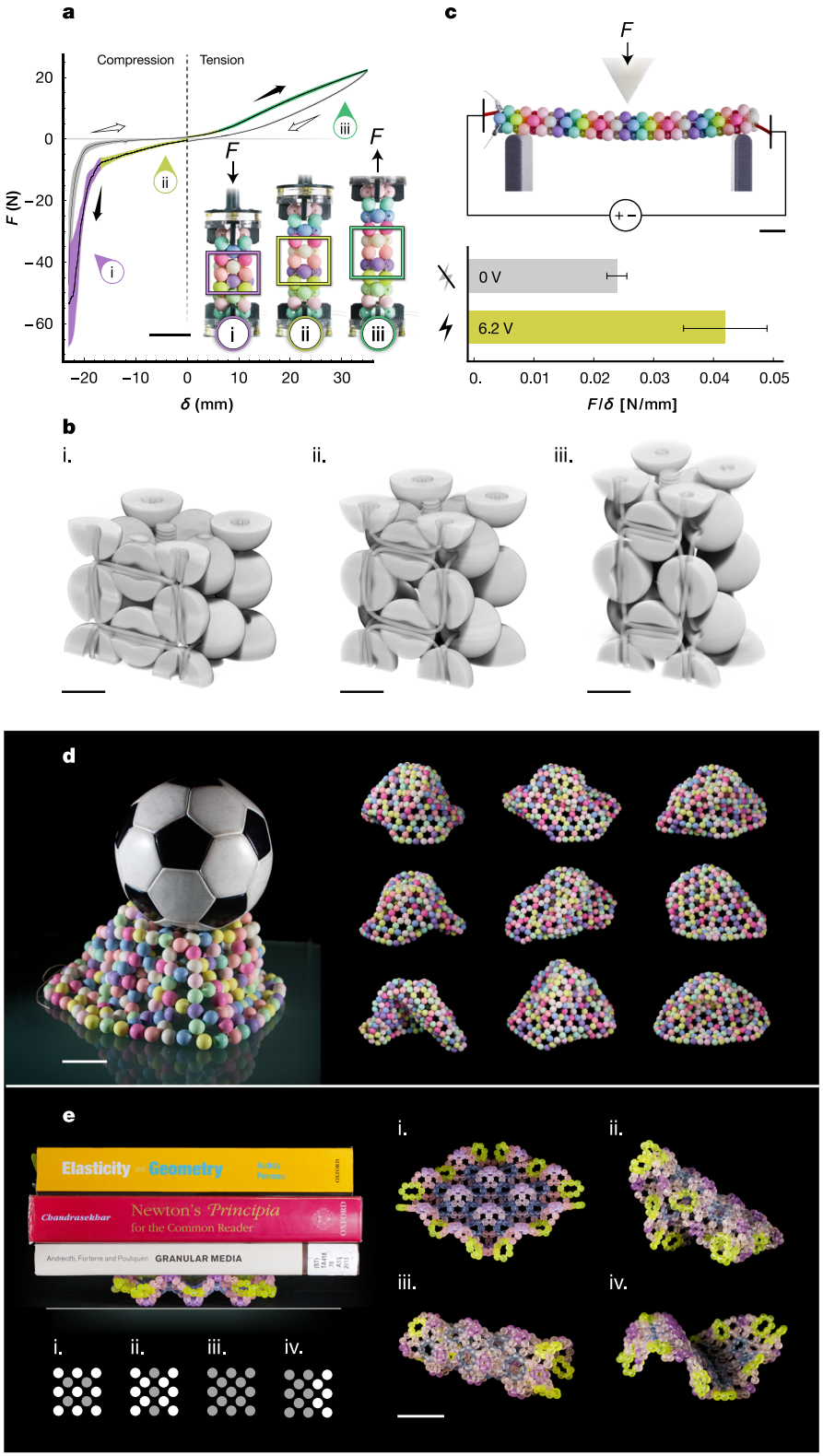

Fig. 4 | Mechanical properties of larger beaded networks. a A beaded column consisting of loops with $n = 4$ and elastomeric thread is stretched and compressed, revealing three regimes: linear elastic (yellow), strain stiffening (green), and super-jamming (purple). Loading and unloading paths are marked with black and white arrows, respectively. Scale bar, 30 mm. **b** μ-CT imaging of the column in **a** with in-situ forcing in the following configurations: jammed (i), neutral (ii), and stretched (iii). Scale bars, 10 mm. **c** A beam beaded with loops of $n = 3$ is threaded with SMA wire, which contracts ~4% when heated by electric current. We perform a 3-point bending test and report the mean fitted slopes (F/δ) for repeated trials, with and without voltage applied. Scale bar, 15 mm. **d** Photograph of a catenary dome beaded using loops of $n = 5$, 6, and 7. The surface is constructed with large acrylic beads ($R = 10$ mm), waxed polyester cord, and is subject to gravity. Bending via the distribution of characteristic slack in the network causes localized stiffening, leading to metastability and many possible rigid conformations. Scale bar, 100 mm. **e** Photograph of a rigid, egg-crate-like surface beaded using loops of $n = 4$, 6, and 8. The surface is constructed with small acrylic beads ($R = 6$ mm). Up and down states are marked in white and gray, respectively. Photographs of the corresponding structures are shown in **i**–**iv**. Scale bar, 30 mm. Source data is available in Supplementary Data 3.

Table 1 | Bead materials used in the study

Material	Dia. (mm)	Hole dia. (mm)	Source	Figure reference
Acrylic, frosted	5.85 ± 0.08	1.81 ± 0.03	Amazon.com	4c, e
Acrylic, frosted	9.60 ± 0.44	2.26 ± 0.13	Amazon.com	1a; 1b ii; 2, SI 2a–b, d; SI Video 1
Acrylic, frosted	11.54 ± 0.06	2.52 ± 0.06	Amazon.com	4a–b
Acrylic, frosted	17.35 ± 0.12	2.45 ± 0.05	Amazon.com	1b i,iii; SI Video 1
Acrylic, frosted	19.29 ± 0.14	2.45 ± 0.05	Amazon.com	4d
Acrylic, smooth	9.80 ± 0.05	2.16 ± 0.05	Amazon.com	3; SI 4
Acetal	25.32 ± 0.00	1.57 ± 0.04	McMaster-Carr (9614K59)	SI 2c
Acetal	19.00 ± 0.01	1.59 ± 0.03	McMaster-Carr (9614K25)	SI 2c
Acetal	12.66 ± 0.00	1.59 ± 0.03	McMaster-Carr (9614K27)	SI 2c
Wood	47.96 ± 0.57	7.28 ± 0.34	Amazon.com	1b iv

Table 2 | Thread materials used in the study

Material	Dia. (mm)	Source	Figure reference
Nitinol	0.25 ± 0.00	McMaster-Carr (3617N26), Component Supply (NW-0100)	1b ii; 2, 3a–c; SI 2; SI 4a–c; SI Video 1
Nitinol	0.20 ± 0.00	McMaster-Carr (3617N24)	3d
Flexinol+ shape-memory nitinol	0.20 ± 0.00	Dynalloy	4c
KastKing monofilament nylon	0.50 ± 0.01	Amazon.com	1a; 2; 3; SI 2a–b, d; SI 4d–h
Coated wire rope	0.76 ± 0.01	McMaster-Carr (34235T26)	1b i, iii; SI Video 1
Coated wire rope	0.81 ± 0.01	McMaster-Carr (34235T27)	1b iv
Beadalon elasticity polyurethane	0.92 ± 0.01	Amazon.com	4a–b
Ritza Tiger waxed nylon	0.42 ± 0.01	Amazon.com	4d

order 2^m metastable states, where m is the number of cones. This system bears many similarities to a well-studied domed metamaterial, in which bistable shell-like features embedded in an elastic material interact with one another when inverted[55,56]. These studies have shown that the buckling threshold is influenced by spacing and material stiffness. In beading, the buckling threshold is more complex because the stiffness is more complex.

In summary, we classify the load-bearing capacity of beaded materials in terms of two principal categories: (1) a first-order mechanical response governed by geometry and tension and (2) nonlinear behaviors such as superjamming and dissipative sliding. The first aspects can be found in other systems, e.g., in tensegrity, but their combination with the second set of properties is unique to beading. In particular, superjamming arises from bead-bead contact and enables significantly higher loads than those in the linear regime, provided the beads can sustain compression and maintain cohesion by friction or some other means to remain locked. In large networks, capstan dissipation can reduce tension to nearly zero, allowing slack to accumulate. Importantly, global failure in complex networks is typically avoided: friction prevents catastrophic unwinding and promotes the dissipation of energy in a distributed manner. We also note that load capacity depends on boundary conditions, though these effects are not explored in detail here. The ability to resist displacement at supports—whether pinned, hinged, or clamped—can likely affect structural integrity.

Methods

Materials

A table listing the materials, dimensions, and sources for bead and thread materials used in this study is provided in Tables 1 and 2.

Dodecahedral shell

Compression experiments. In Fig. 1b iii, the thread ends were manually tensioned and then clamped to a rigid support, as illustrated in Fig. SI 2d, inset. Thread ends are not visible in the image. Both photographs in Fig. 1b ii and iii were taken on a background that was removed. A gray gradient was added at the shell bases.

Details of the experimental setups used to obtain data reported in Fig. 2b–d are illustrated in Fig. SI 1. The setup was fitted with two pulleys and a 45° angled mirror positioned beneath a transparent acrylic stage. Masses ranging from 200 to 800 g were attached to both thread ends, causing the shell to pop out-of-plane due to the closing of the bottom loop with tension. The shell was compressed for three cycles per tension trial using a 3D-printed polylactic acid (PLA) compression plate. Force vs. displacement data was recorded using a universal testing machine (Instron 5940).

Tracking bead motion. While the shells were compressed, bead positions from the front and bottom were recorded using a digital camera. To obtain the measurements reported in Fig. 2e, f motion tracking for a single cycle was performed on bead centers using Adobe After Effects (Adobe Inc.). Force and RGB data were synchronized with the starting motion of the compression plate. To measure dilation ($\Delta\epsilon_{avg}$), we fitted circles through the bottom bead centers at each frame, obtaining an approximate dilation radius, R. Subtracting the thread length inside of the beads, we found $\Delta\epsilon$ at each video frame such that

$$\Delta\epsilon_{avg} = \frac{2\pi R - nr^*}{m}, \tag{2}$$

where $r^* = 9.2$ mm is the average bead diameter taken across bead holes, $n = 10$ is the number of beads in the lower ring, and $m = 5$ is the number of loops encircling the central loop (yellow beads).

To measure out-of-plane deformation, we tracked x–y–z positions of bead centers in a sample unit cell, taking the mean of the two x-values obtained from front and bottom views. Angles θ_1 and θ_2 are calculated by taking the mean of the vectors constructed from the blue bead center to each pair of top and bottom bead centers (yellow and pink). For both measurements, we report the altitudinal angle, i.e., the angle formed between these vectors and the x–y plane.

To find $F_{\|}$, we also accounted for in-plane spreading of the pink beads, i.e. α, as illustrated in Fig. 2e. The evolution of α is not shown in Fig. 2g, but was derived from the vectors used to compute θ_2, taking 1/

2 the angle formed by their projections in the x–y plane. We thus recast F, θ_2, and α as functions of $\Delta\epsilon_{avg}$ and applied the following geometric relation:

$$F_{\parallel} = \frac{F}{m \tan\theta_2 \sin\alpha}, \tag{3}$$

where F is modulated by angular contacts across $m = 5$ building blocks, noting that the effect of α on $F_{\parallel}$ is minimal ($\sin\alpha \approx 0.9$–1.0).

Nitinol and nylon characterization

Effective sliding friction, μ_{eff}. Rings of n beads were threaded with nitinol and nylon as illustrated in Fig. SI 1c. Each assembly was secured between two 3D-printed PLA clamps designed with hemispherical groves so that the thread could pass unobstructed through the assembly, but the beads remained fixed to the experimental setup when tension was applied. One end of the thread was fed through a frictionless pulley where masses were attached (50–500 g in increments of 50 g). The other end was fed through another frictionless pulley and passed upwards to a clamp attached to a universal testing machine. The thread at the sensor was moved upwards at 30 mm/s, and we recorded the tension vs. displacement at this end. We repeated the experiment across bead assemblies of different sizes: $n = 3$, 4, 5, and 6.

Young's modulus, E. We measured the force F to stretch thread samples of different lengths a distance δ axially when secured between two clamps. Trials were conducted with clamps spaced 10, 25, 50, and 100 mm apart, with three trials performed at each distance. To find Young's modulus E, we extracted a slope s fitted to the elastic regime of each F vs. δ displacement curve. We then calculated E such that $E = sL_0/A$, where A is the unstretched thread cross-section and L_0 incorporates a fitted, additional length assumed to be stretching inside of each clamp (13 and 9 mm for nitinol and nylon, respectively, per clamp). Reporting the mean E across samples, we obtained 38.2 ± 3.2 and 1.80 ± 0.13 GPa for nitinol and nylon, respectively. We note that both materials remained linearly elastic until $\delta/L_0 \approx 0.015$.

Ring dilation

Experiments. To obtain the dilation data shown in Fig. 3c, we assembled beaded rings identical to those tested in Fig. 3a, b and measured the force to dilate the rings using a spherically-tipped indenter (see Fig. SI 1b), cycling three times for a range of pretensions ($T_0 = 2.0$–9.8 N). In Fig. 3d, we constructed a chain of $m = 15$ unit cells where $n = 4$ via a two-handed right-angle-weave (RAW) design. Bead rings are linked by a single common bead, and two thread ends are worked in an alternating fashion such that the thread snakes through the weave on alternating sides of each ring. In this manner, the thread accumulates a capstan wrapping angle of $\phi = \pi$ per ring. In Fig. SI 4g we show a μ-CT section cut through a RAW chain where $m = 8$. To dilate the chain, a similar approach was used as described previously, using a spherical-tipped indenter. The chain was dilated sequentially starting at the free end ($m = 1$), moving towards $m = 15$ (see Fig. SI 1d), performing three dilation cycles per ring over a range of T_0 as reported in Fig. 3d.

Model. We dilate a ring of n beads with radius a with a spherical indenter of the same radius. The geometric relationship between indenter displacement δ and the altitudinal angle θ is described as

$$\delta = 2a(1 - \sin\theta), \tag{4}$$

where θ is defined as the angle between the line connecting the indenting sphere center and the center of a bead in the ring and the x–y plane. The transfer of vertical force to the bead ring occurs through bead contacts such that

$$\frac{F}{n} = F_n \sin\theta, \tag{5}$$

where F_n represents the contact force between a single bead and the indenter. Projected in the x–y plane, the component dilation force $F_n \cos\theta$ is resisted by threads that emerge from bead holes at an angle β. We proceed with the assumption that tension in the thread is constant and, as a result, that the ring deforms with radial symmetry. In static equilibrium, we can write the balance of in-plane forces along radial lines of symmetry as

$$2T\cos\beta = F_n \cos\theta, \tag{6}$$

where β is constant due to assumed symmetry and can be derived from the regular polygon formed by discrete bead edges, such that $\beta = \frac{\pi}{2} - \frac{\pi}{n}$. We solve this system of three equations and plot the results in Fig. 3c.

To overlay experimental data with the model, we define our reference for $\delta = 0$ by assuming the point of maximum force occurs when the indenter makes contact with a perfectly taut bead ring. In-plane, we can describe the radius R of a circle that intersects the centers of a taut loop of n beads as

$$R = \frac{a}{\sin(\pi/n)}. \tag{7}$$

Out-of-plane, we can thus write the contact height $h = 2a - \delta$ of the indenting sphere as

$$h = a\left(4 - \frac{1}{\sin^2(\pi/n)}\right)^{1/2}. \tag{8}$$

Larger bead network experiments

Column beaded with elastomeric thread. We used a "prismatic right-angle weave (PRAW) technique to achieve the columnar geometry, consisting of angle weave loops of $n = 4$ oriented vertically. These loops are constructed around an initial ring of a given size—here, also $n = 4$—making this a PRAW-4 design. We constructed 11 layers using 12-mm acrylic beads with elastomeric thread (see Tables 1 and 2) to create a square prism, 92 mm long at rest length. We manually tensioned the thread at the free end and tied a knot to maintain tension. The column was secured to a universal testing machine using a custom clamping apparatus (3D printed PETG, laser-cut acrylic, hardware) that grips the end beads but not the thread (see Fig. 4a, inset). We recorded the force to compress and extend the column, cycling three times over a total displacement of 35 mm extension and 23 mm compression at 30 mm/min.

Beam beaded with SMA wire. We beaded a beam using a PRAW-3 design (see above) consisting of 31 layers of 6-mm acrylic beads and shape-memory nitinol (see Tables 1 and 2) to create a triangular prism, 125 mm long at rest length. We manually tensioned the thread at the free end and applied metal crimps to maintain tension. Alligator clips connected to a benchtop power supply were connected to exposed nitinol at both beam ends. The "on" voltage setting (6 V) was selected by increasing the voltage at the power supply until the current draw reached the maximum value recommended by the manufacturer per the wire diameter (660 mA)[50]. We then conducted 3-point bending tests in both "off" and "on" states, cycling a total of 9 and 12 times, respectively, at 30 mm/min. Linear models were fitted to the resulting force vs. displacement plots.

Catenary shell. A catenary shell geometry was generated in 3D modeling software (*Rhino/Grasshopper*, Robert McNeel & Associates). We then constructed a triangular mesh with optimized edge lengths by packing spheres of equal radii on this surface[57] and connecting each point to six nearest neighbors. We placed beads at mesh face centers to generate a beadable pattern, which was then assembled by hand using 20-mm acrylic beads and a waxed, filamentous nylon thread (see Tables 1 and 2). In the photographs of Fig. 4d, the shell was manipulated into different conformations and set to rest with gravity. The shell was photographed on a black background that was removed.

Tomography

μ-CT imaging in Figs. 1b ii, 4b, and SI 4a–g was conducted using a Zeiss Xradia Versa 520 3D X-ray microscope. Tension was applied to threads by manually pulling the ends and tying a knot. Tomography data was rendered using Dragonfly 3D visualization software (Comet Technologies). Figure 4b (beaded column) and Figs. SI 4a–c (nitinol samples) show 3D rendered orthographic views of a cropped region of interest. Figure SI 4d–g (nylon samples) uses a mean slab section cut across a thickness of ~1 mm.

Data availability

Source data are provided with this paper as supplementary information.

References

1. Banerjee, P. K. *Principles of Fabric Formation* (CRC Press, 2014).
2. Bertoldi, K., Vitelli, V., Christensen, J. & Van Hecke, M. Flexible mechanical metamaterials. *Nat. Rev. Mater.* **2**, 1–11 (2017).
3. Reis, P. M. A perspective on the revival of structural (in)stability with novel opportunities for function: from buckliphobia to buckliphilia. *J. Appl. Mech.* **82**, 111001 (2015).
4. Holmes, D. P. Elasticity and stability of shape-shifting structures. *Curr. Opin. Colloid Interface Sci.* **40**, 118–137 (2019).
5. Keim, N. C., Paulsen, J. D., Zeravcic, Z., Sastry, S. & Nagel, S. R. Memory formation in matter. *Rev. Mod. Phys.* **91**, 035002 (2019).
6. Poincloux, S., Adda-Bedia, M. & Lechenault, F. Geometry and elasticity of a knitted fabric. *Phys. Rev. X* **8**, 021075 (2018).
7. Patil, V. P., Sandt, J. D., Kolle, M. & Dunkel, J. Topological mechanics of knots and tangles. *Science* **367**, 71–75 (2020).
8. Jawed, M. K., Dieleman, P., Audoly, B. & Reis, P. M. Untangling the mechanics and topology in the frictional response of long overhand elastic knots. *Phys. Rev. Lett.* **115 11**, 118302 (2015).
9. Warren, P. B., Ball, R. C. & Goldstein, R. E. Why clothes don't fall apart: tension transmission in staple yarns. *Phys. Rev. Lett.* **120**, 158001 (2018).
10. Baek, C., Sageman-Furnas, A. O., Jawed, M. K. & Reis, P. M. Form finding in elastic gridshells. *Proc. Natl Acad. Sci. USA* **115**, 75–80 (2018).
11. Moestopo, W. P., Mateos, A. J., Fuller, R. M., Greer, J. R. & Portela, C. M. Pushing and pulling on ropes: hierarchical woven materials. *Adv. Sci.* **7**, 2001271 (2020).
12. Yu, T. et al. Numerical modeling of static equilibria and bifurcations in bigons and bigon rings. *J. Mech. Phys. Solids* **152**, 104459 (2021).
13. Poincloux, S., Vallat, C., Chen, T., Sano, T. G. & Reis, P. M. Indentation and stability of woven domes. *Extrem. Mech. Lett.* **59**, 101968 (2023).
14. Kabla, A. & Mahadevan, L. Nonlinear mechanics of soft fibrous networks. *J. R. Soc. Interface* **4**, 99–106 (2007).
15. Andrade-Silva, I., Godefroy, Théo, Pouliquen, O. & Marthelot, J. Cohesion of bird nests. *EPJ Web Conf.* **249**, 06014 (2021).
16. Dumont, D. et al. Emergent strain stiffening in interlocked granular chains. *Phys. Rev. Lett.* **120**, 088001 (2018).
17. Xiong, J., Chen, J. & Lee, P. S. Functional fibers and fabrics for soft robotics, wearables, and human–robot interface. *Adv. Mater.* **33**, 2002640 (2021).
18. Sanchez, V., Walsh, C. J. & Wood, R. J. Textile technology for soft robotic and autonomous garments. *Adv. Funct. Mater.* **31**, 2008278 (2021).
19. Tonazzini, A. et al. Variable stiffness fiber with self-healing capability. *Adv. Mater.* **28**, 10105 (2016).
20. Chen, Y. et al. Controlled flight of a microrobot powered by soft artificial muscles. *Nature* **575**, 324–329 (2019).
21. Zhai, Z., Wu, L. & Jiang, H. Mechanical metamaterials based on origami and kirigami. *Appl. Phys. Rev.* **8**, 041319 (2021).
22. Meeussen, A. & van Hecke, M. Multistable sheets with rewritable patterns for switchable shape-morphing. *Nature* **621**, 516–520 (2023).
23. Kuder, I. K., Arrieta, A. F., Raither, W. E. & Ermanni, P. Variable stiffness material and structural concepts for morphing applications. *Prog. Aerosp. Sci.* **63**, 33–55 (2013).
24. Blanc, L., Delchambre, A., & Lambert, P. Flexible Medical Devices: Review of Controllable Stiffness Solutions. *Actuators*, **6**, 23 (2017).
25. Hao, Y., Gao, J., Lv, Y. & Liu, J. Low melting point alloys enabled stiffness tunable advanced materials. *Adv. Funct. Mater.* **32**, 2201942 (2022).
26. Liu, A. J. & Nagel, S. R. Jamming is not just cool any more. *Nature* **396**, 21–22 (1998).
27. Majmudar, T., Sperl, M., Luding, S. & Behringer, R. P. Jamming transition in granular systems. *Phys. Rev. Lett.* **98**, 058001 (2007).
28. Bakarich, S. E. et al. Pump up the jam: Granular media as a quasi-hydraulic fluid for independent control over isometric and isotonic actuation. *Adv. Sci.* **9**, 2104402 (2022).
29. Brown, E. et al. Universal robotic gripper based on the jamming of granular material. *Proc. Natl Acad. Sci. USA* **107**, 18809–18814 (2010).
30. Wang, Y., Li, L., Hofmann, D., Andrade, J. E. & Daraio, C. Structured fabrics with tunable mechanical properties. *Nature* **596**, 238–243 (2021).
31. Guerra, A. & Holmes, D. P. Emergence of structure in columns of grains and elastic loops. *Soft Matter* **17**, 7662–7669 (2021).
32. Haver, D. et al. Elasticity and rheology of auxetic granular metamaterials. *Proc. Natl Acad. Sci.* **121**, e2317915121 (2024).
33. Shah, D. S. et al. Tensegrity robotics. *Soft Robot.* **9**, 639–656 (2022).
34. Rivas, A. E. Tensegrity. In *Deployable Structures* 90–101 (Laurence King Publishing, London, 2015).
35. Connelly, R. Tensegrity structures: why are they stable? In *Rigidity Theory and Applications* (eds Thorpe, M. F. & Duxbury, P. M.) 47–54 (Kluwer Academic Publishers, New York, 2002).
36. Liu, K. & Paulino, G. H. Tensegrity topology optimization by force maximization on arbitrary ground structures. *Struct. Multidiscip. Optim.* **59**, 2041–2062 (2019).
37. Fu, K., Zhao, Z. & Jin, L. Programmable granular metamaterials for reusable energy absorption. *Adv. Funct. Mater.* **29**, 1901258 (2019).
38. Chuang, C. et al. Molecular modeling of fullerenes with beads. *J. Chem. Educ.* **89**, 414–416 (2012).
39. Fisher, G. L. & Mellor, B. Using tiling theory to generate angle weaves with beads. *J. Math. Arts* **6**, 141–158 (2012).
40. Fisher, G. L. Highly unlikely triangles and other impossible figures in bead weaving. In *Proc. Bridges 2015: Mathematics, Music, Art, Architecture, Culture* (eds Delp, K., Kaplan, C. S., McKenna, D. & Sarhangi, R.) 99–106 (Tessellations Publishing, Phoenix, AZ, 2015).
41. Tsoo, C.-C. & Jin, B.-Y. Designing skeletal polyhedral sculptures inspired by octet-truss systems and structural inorganic chemistry with bugle beads. In *Proc. Bridges 2017: Mathematics, Art, Music, Architecture, Education, Culture* (eds Swart, D., Séquin, C. H. & Fenyvesi, K.) 483–486 (Tessellations Publishing, Phoenix, AZ, 2017).

42. Barbier, C., Dendievel, R. & Rodney, D. Role of friction in the mechanics of nonbonded fibrous materials. *Phys. Rev. E* **80**, 016115 (2009).
43. Persson, B. N. J. *Sliding on Clean (Dry) Surfaces* 93–100 (Springer, Berlin, Heidelberg, 2000).
44. Euler, L. Remarques sur l'effet du frottement dans l'equilibre. *Mem. Acad. Sci. Berlin* 265–278 (1769).
45. Eytelwein, J. A. *Handbuch der Statik fester Körper: mit vorzüglicher Rücksicht auf ihre Anwendung in der Architektur*, Vol. 1 (De Gruyter, Incorporated, 1832).
46. Grandgeorge, P., Sano, T. G. & Reis, P. M. An elastic rod in frictional contact with a rigid cylinder. *J. Mech. Phys. Solids* **164**, 104885 (2022).
47. Jung, J. H., Pan, N. & Kang, T. J. Capstan equation including bending rigidity and non-linear frictional behavior. *Mech. Mach. Theory* **43**, 661–675 (2008).
48. Winer, J. P., Oake, S. & Janmey, P. A. Non-linear elasticity of extracellular matrices enables contractile cells to communicate local position and orientation. *PLoS ONE* **4**, 1–11 (2009).
49. Rouse, J. & Prince, E. A theory of the linear viscoelastic properties of dilute solutions of coiling polymers. *J. Chem. Phys.* **21**, 1272–1280 (1953).
50. DYNALLOY, Inc. *Flexinol® Actuator Wire Technical and Design Data*. https://www.dynalloy.com/tech_data_wire.php (2024).
51. Audoly, B. & Pomeau, Y. Elasticity and Geometry: From Hair Curls to the Non-linear Response of Shells. https://books.google.com/books?id=FMQRDAAAQBAJ (OUP Oxford, 2010).
52. Liu, J. et al. Shaping and locomotion of soft robots using filament actuators made from liquid crystal elastomer–carbon nanotube composites. *Adv. Intell. Syst.* **2**, 1900163 (2020).
53. Xu, X. et al. Reconstructed hierarchically structured keratin fibers with shape-memory features based on reversible secondary-structure transformation. *Adv. Mater.* **35**, 2304725 (2023).
54. Boni, C. & Royer-Carfagni, G. A nonlocal elastica inspired by flexural tensegrity. *Int. J. Eng. Sci.* **158**, 103421 (2021).
55. Plummer, A. & Nelson, D. R. Buckling and metastability in membranes with dilation arrays. *Phys. Rev. E* **102**, 033002 (2020).
56. Liu, M., Domino, L., de Dinechin, I. D., Taffetani, M. & Vella, D. Snap-induced morphing: from a single bistable shell to the origin of shape bifurcation in interacting shells. *J. Mech. Phys. Solids* **170**, 105116 (2023).
57. Piker, D. *Circlepackonsurface.gh* https://github.com/Dan-Piker/Kangaroo-examples/blob/master/collisions_and_packing/CirclePackOnSurface_pull.gh (2017).

Acknowledgements

This work was supported by NSF Future Manufacturing Grant CMMI 2037097. We would like to thank ballet dancer Gigi Schadrack for standing on the experiments in Fig. 1b iii–iv. T.J.J. would like to thank Tracey Jones for introducing him to the art of bead-weaving.

Author contributions

L.D., T.J.J. and P.-T.B. designed the research. L.D. performed the research, and A.P. and T.J.J contributed to some experiments. All the authors analyzed the data. L.D. wrote the paper. All the authors edited the manuscript. A.K. and P.-T.B. advised L.D.

Competing interests

The authors declare no competing interests.

Additional information

Supplementary information The online version contains supplementary material available at https://doi.org/10.1038/s41467-025-61809-8.

Correspondence and requests for materials should be addressed to P.-T. Brun.

Peer review information *Nature Communications* thanks Viacheslav Slesarenko, who co-reviewed with Naeim Ghavidelnia, and Jie Yin and Corentin Coulais for their contribution to the peer review of this work. A peer review file is available.

Reprints and permissions information is available at http://www.nature.com/reprints

Publisher's note Springer Nature remains neutral with regard to jurisdictional claims in published maps and institutional affiliations.

Open Access This article is licensed under a Creative Commons Attribution-NonCommercial-NoDerivatives 4.0 International License, which permits any non-commercial use, sharing, distribution and reproduction in any medium or format, as long as you give appropriate credit to the original author(s) and the source, provide a link to the Creative Commons licence, and indicate if you modified the licensed material. You do not have permission under this licence to share adapted material derived from this article or parts of it. The images or other third party material in this article are included in the article's Creative Commons licence, unless indicated otherwise in a credit line to the material. If material is not included in the article's Creative Commons licence and your intended use is not permitted by statutory regulation or exceeds the permitted use, you will need to obtain permission directly from the copyright holder. To view a copy of this licence, visit http://creativecommons.org/licenses/by-nc-nd/4.0/.

© The Author(s) 2025

Supplementary Information

Beaded metamaterials

Lauren Dreier[1], Trevor J. Jones[2], Abigail Plummer[3], Andrej Košmrlj[3,4], P.-T. Brun[2,5*]

[1]*School of Architecture,* [2]*Department of Chemical and Biological Engineering,*
[3]*Department of Mechanical and Aerospace Engineering,* [4]*Princeton Materials Institute, Princeton University, Princeton, New Jersey 08540, USA,*
[5]*KU Leuven, Department of Chemical Engineering, Soft Matter, Rheology and Technology, 3001 Leuven, Belgium*

[*]pierre-thomas.brun@kuleuven.be

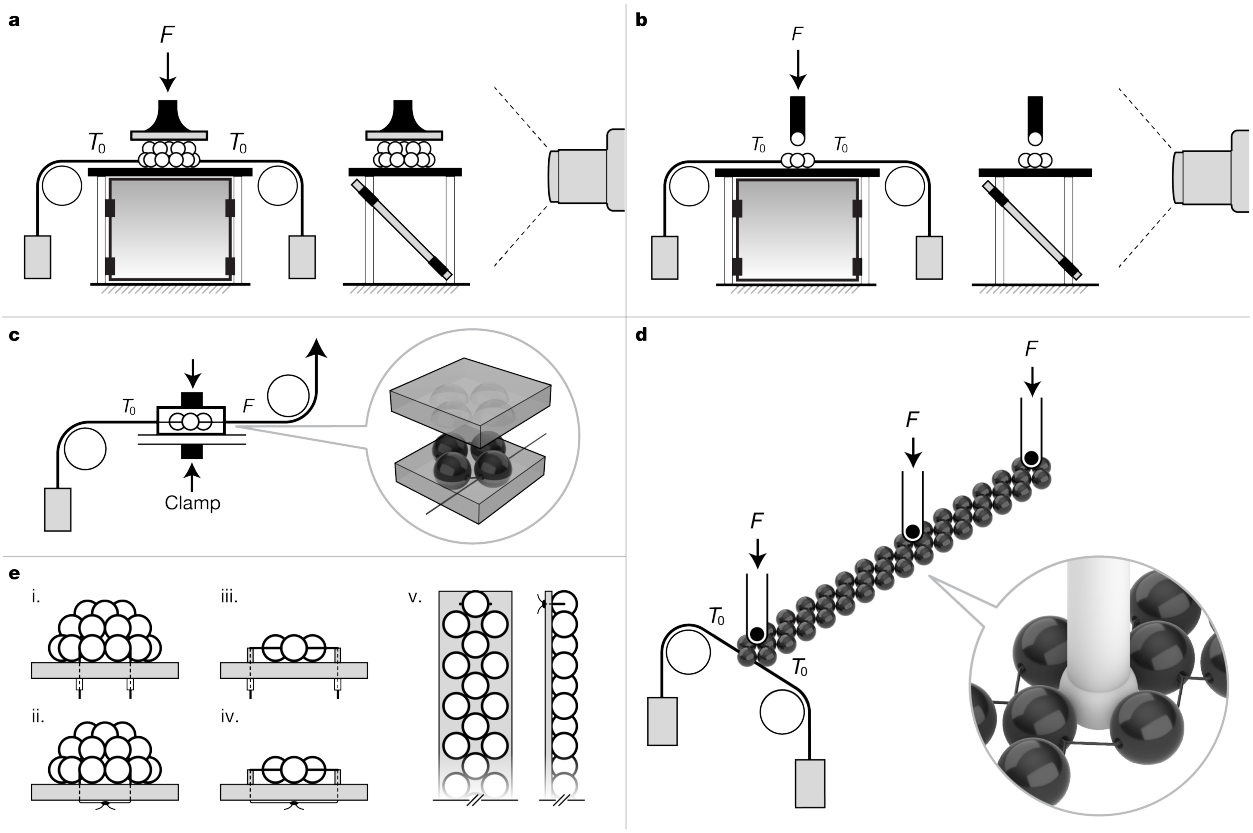

Fig. SI 1: **Experimental setups details. a**, Angled mirror setup for shell compression experiment. **b**, Angled mirror setup for ring dilation experiment. **c**, Measuring capstan friction in a planar ring. Inset shows 3D printed housing into which the ring is inserted (3D rendering); then the assembly is clamped to the experimental stage. **d**, Dilation of a beaded chain where $n = 4$ and $m = 15$. Inset shows the spherical-tipped indenter (3D rendering). **e**, Tomography setups for the shell (i, ii), rings (iii, iv), and chain where $m = 8$ (v), showing clamping techniques. Bead assemblies threaded with nitinol are manually tensioned and crimps are applied to each end. In the case of nylon, the thread is manually tensioned, tied, and glued to prevent slipping. In all cases, the thread is passed through a polymeric platform (3D printed PLA, PETG, or laser-cut acrylic) such that knotting/crimping is performed on the underside. After tensioning, the bead assemblies are glued to the platform.

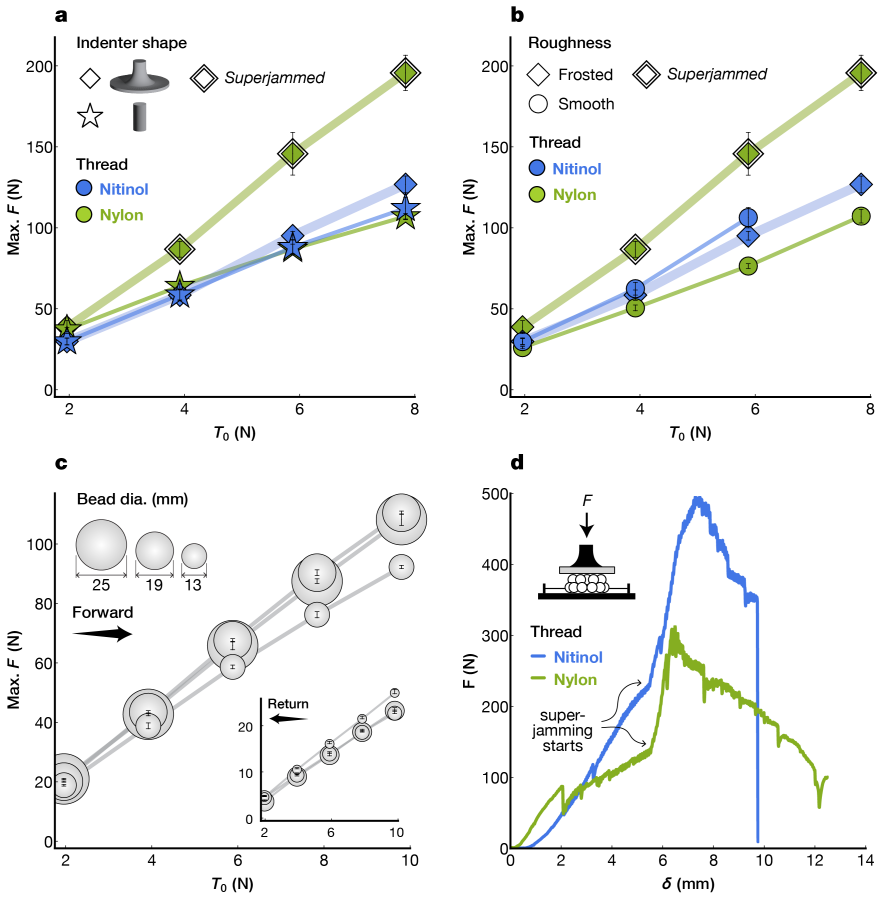

Fig. SI 2: **Maximum loads of bead shells. a**, The effect of indenter shape was tested in shells made from frosted, 10-mm acrylic beads threaded with nitinol (blue) and nylon (green), using plate-shaped (diamond) and columnar (star) indenters, where the diameter of the column (17 mm) spans the centers of the upper ring (yellow beads) and does not come into contact with other beads. We report the maximum load across a range of pretensions ($T_0 = 2.0 - 7.8$ N). The results from Fig. **??**d are highlighted with thick lines. A plate indenter was used for all of the following experiments. **b**, The effect of bead roughness was tested in shells made with 10-mm smooth (circle) and rough i.e. frosted (diamond) acrylic beads threaded with nitinol (blue) and nylon (green). We report the maximum load across a range of pretensions ($T_0 = 2.0 - 7.8$ N). The results from Fig. **??**d are highlighted with thick lines. **c**, The effect of bead size was tested in shells made with smooth acetal spheres threaded with nitinol and manually drilled to maintain consistent bead hole geometry. We report the maximum load across a range of pretensions ($T_0 = 2.0 - 9.8$ N). Inset shows the maximum load during the return. **d**, In lieu of pretension supplied by a sliding weight-and-pulley system, here we manually pretension thread ends and clamp them. We report force vs. indenter displacement until failure for shells made with 10-mm frosted acrylic beads threaded with nitinol (blue) and nylon (green). The slopes in the superjammed regime are 170 and 193 N/mm for nitinol and nylon, respectively.

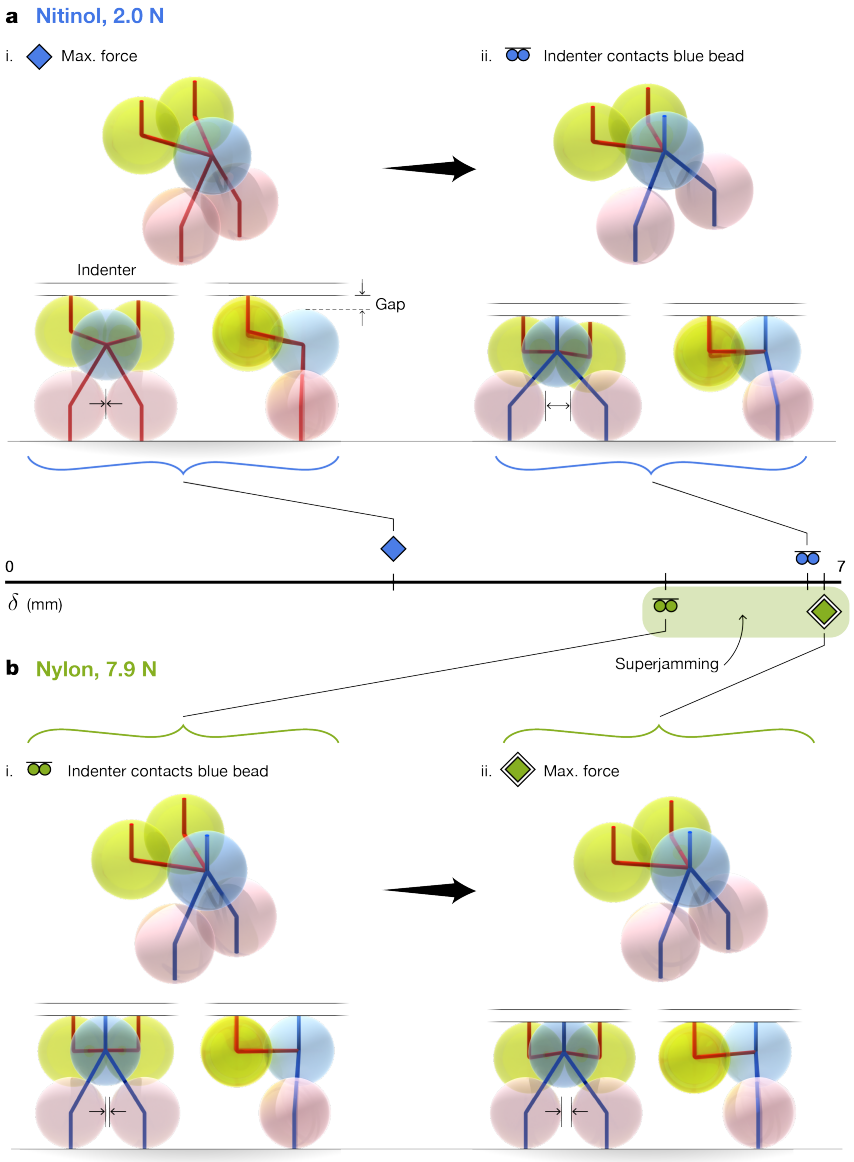

Fig. SI 3: **3D reconstruction of motion-tracked bead centers.** **a–b**, Conformations of the 5-bead building block are rendered for shells threaded with nitinol and nylon, tensioned with 2.0 N and 7.9 N, respectively. Red and blue lines show the force path, where the indenter contacts the structure at the upper (yellow) and middle (blue) beads, respectively. Superjamming occurs in **b**. The blue force path is nearly vertical, and the pink beads separate minimally.

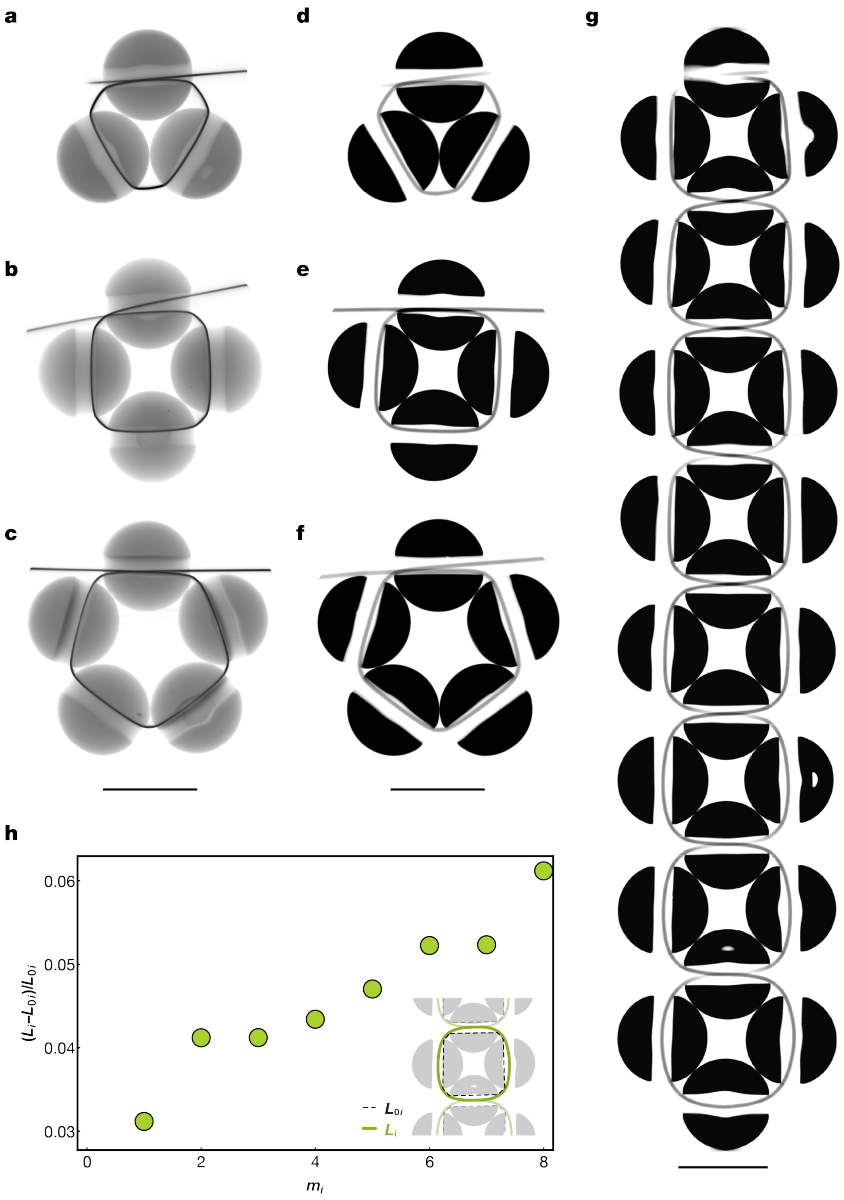

Fig. SI 4: **Section cuts through angle weave unit cells.** **a–f**, Section cuts made through μ-CT data at the center of unit cells threaded with nitinol (a, b c) and nylon (d, e, f) for $n = 3, 4$ and 5, respectively. Scale bars, 10 mm. **g**, Continuous chain of $m = 8$ unit cells for $n = 4$, threaded with nylon. Scale bar, 10 mm. **h**, Nondimensional thread length measured for each ring of panel g.

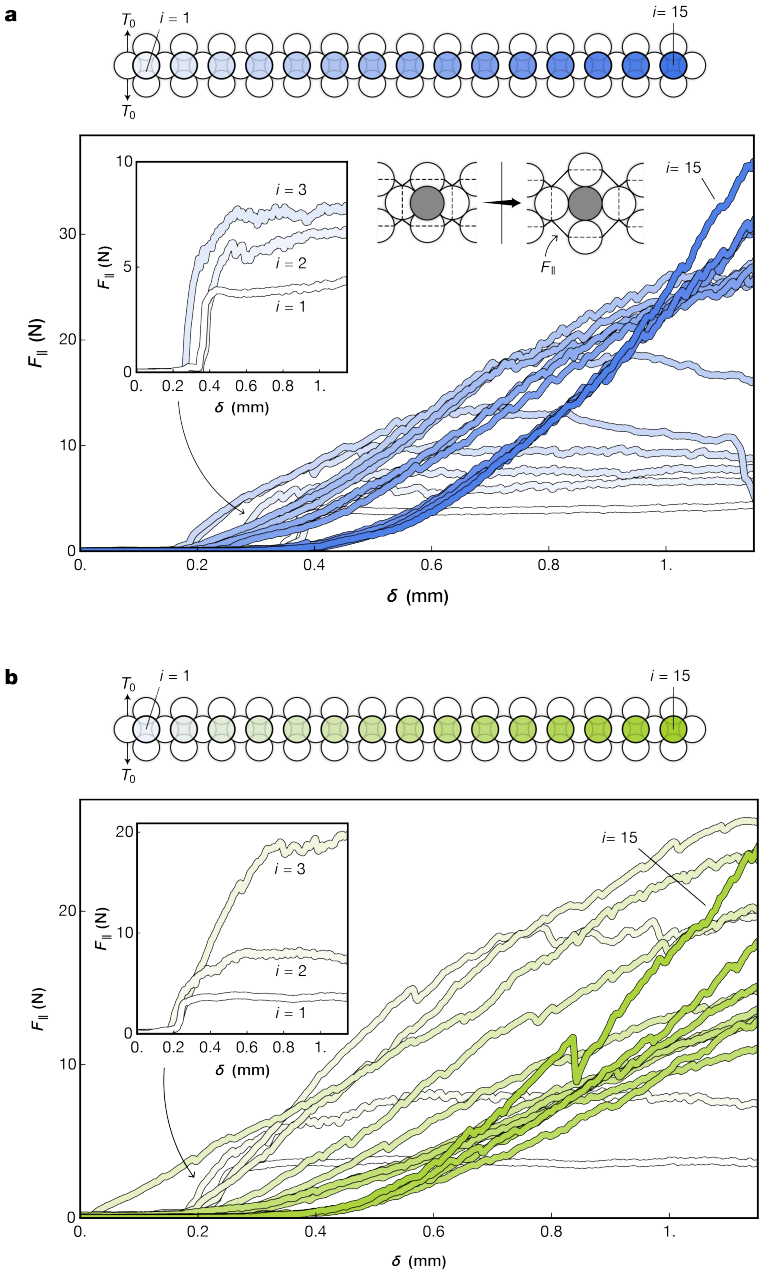

Fig. SI 5: **Projected force to dilate cells in a beaded chain. a–b**, A chain of 15 rings with $n = 4$ beads per ring is dilated sequentially with a spherical indenter starting at $i = 1$. We report the in-plane projected force $F_\parallel$ as illustrated in a, inset. Results are shown for chains with $T_0 = 2.0$ N, threaded with nitinol and nylon in a and b, respectively. For clarity, inset plots of a and b show the projected force for the three rings closest to the free end.

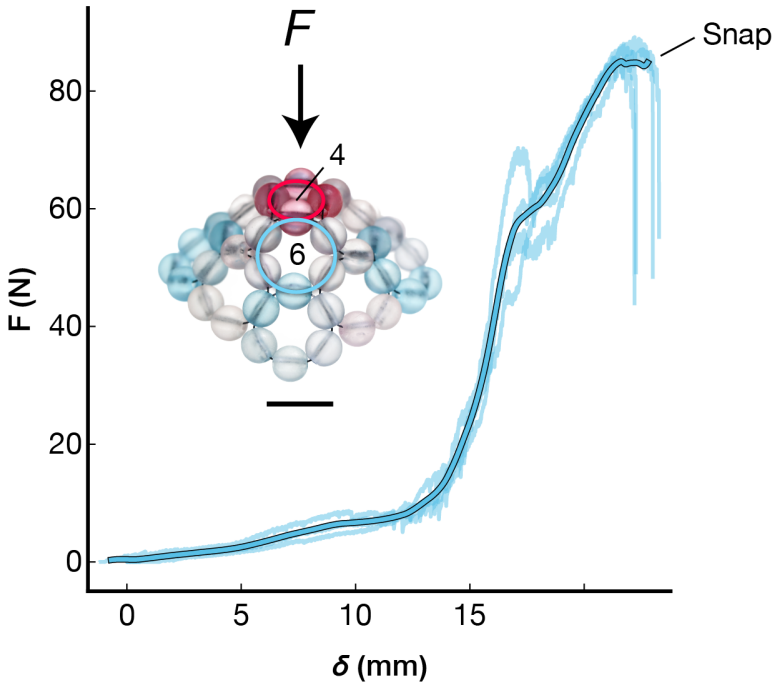

Fig. SI 6: **Force to snap a D-cone between its two configurations.** The D-cone was threaded with nylon, manually pretensioned, and free ends tied. A point load was applied to the defect loop ($n = 4$, red beads) until the cone reversed orientation. The outlined curve shows the moving average across four cycles. Scale bar, 20 mm.